Advanced Materials

ADVANCED MATERIALS
www.advmat.de

RESEARCH ARTICLE OPEN ACCESS

Quantitative 3D Real-Space Analysis of Photonic Supraparticles

Jesse Ian Bückmann | Leroy Daniël Hoitink | Ruizhi Yang | Alptuğ Ulugöl | Laura Filion | Alfons van Blaaderen

Soft Condensed Matter and Biophysics Group, Debye Institute for Nanomaterials Science, Utrecht University, Utrecht, Netherlands

Correspondence: Jesse Ian Bückmann (j.i.buckmann@uu.nl) | Alfons van Blaaderen (a.vanblaaderen@uu.nl)

Received: 11 November 2025 | **Revised:** 23 January 2026 | **Accepted:** 13 February 2026

Keywords: confocal microscopy | real-space | self-assembly | supraparticles

ABSTRACT

Supraparticles (SPs) are assemblies of smaller particles, and they form an interesting material class. One way through which these structures can be formed is self-assembly (SA) in spherical confinement, and what makes them unique is that they combine the properties of the smaller particles with collective properties arising from the length scale on which these smaller particles are ordered. Additionally, the limited number of particles in an SP enables them to form structures that are not found in bulk systems. An example of this is icosahedral symmetry, which is the equilibrium structure for SPs up to several hundreds of thousands of particles. Although these icosahedral structures have been investigated through computer simulations and several experimental techniques have been used to analyze them in 3D, the number of experimental datasets published is so limited that no statistically relevant conclusions have been drawn so far. The experimental technique most commonly applied to study them is scanning electron microscopy (SEM), but with this, only quantitative information about the surface of the SPs can be obtained. By using a combination of 3D confocal and stimulated emission depletion (STED) microscopy on extremely well-index-matched (within 0.002) fluorescent core-shell, colloidal silica spheres (of 442–478 nm in diameter with polydispersities below 1%), we obtained full 3D real-space datasets of tens of SPs within several hours. The structures were classified based on bond order parameters and deviations from local centrosymmetry, using an unsupervised machine learning model. From this, we are able to correctly classify structures that are commonly misidentified using SEM. Additionally, the quantitative real-space analysis gave experimental insights into the SA pathway and defect formation mechanisms of mostly icosahedral SPs.

1 | Introduction

It is well known that the equilibrium crystal phase of hard spheres is the face-centered-cubic (FCC) structure, which also maximizes the packing [1]. Interestingly, however, when these same hard spheres are placed in spherical confinement, the situation becomes much more complex [2–5]. In fact, the equilibrium structure (up to on the order of 100 000 particles) becomes a structure that cannot even exist in bulk: an icosahedral arrangement of spheres [6–9]. While this phase has been shown via free-energy calculations to be thermodynamically stable, it does not correspond to the best-packed structure [10]. Note that this prediction is not purely a theoretical concept: nanoparticles and colloids dispersed in emulsion droplets that are then dried have indeed been found to form these structures [6–11].

However, in colloidal systems, it is important to note that many different parameters can affect the resulting self-assembled

---

Jesse Ian Bückmann, Leroy Daniël Hoitink, and Ruizhi Yang contributed equally to this work.

structure. First, while hard spheres are an excellent starting point for predicting what forms experimentally, synthesized nanoparticles and colloids are typically slightly soft (due, e.g., to steric and/or screened charge interactions). A second parameter that will play an important role is the drying rate, because arriving at the free-energy minimum takes time. From simulations, we know that when drying rates are sufficiently slow, the full crystallization pathway can occur undisturbed. This crystallization pathway consists of multiple steps. First, small crystalline domains form on the surface that then grow toward the center of the confinement, forming FCC-like ('Mackay') tetrahedra and bulk icosahedral ordering. Second, the crystal layers at the surface melt and reorganize into surface reconstructed (anti-Mackay) outer termination [6, 8, 10, 12]. However, if the drying speed is too fast, different pathways and structures form. At the fastest drying rates, disordered glassy structures form because the particles lack sufficient time to order. At intermediate drying rates, "onion-shell" structures emerge. Here, the interior may be disordered or icosahedrally ordered, while the outer layers consist of hexagonally ordered concentric crystalline shells [6, 12, 13].

Despite the relevance of SPs in diverse applications [14, 15], ranging from catalytic supports [16] to photonic materials [17, 18], the full 3D real-space structure of SPs has not yet been investigated in detail experimentally [8, 9, 17, 19]. The main reason for this lies in the difficulty of observing the internal structure of the SPs. To date, in real-space these structures have been analyzed using electron tomography [17, 20], where the acquisition and reconstruction of a single dataset is rather time-intensive. As such, these techniques are not suitable to obtain statistically relevant results [21]. The same can also be said for other techniques that have been used over the last few decades to obtain real-space information of colloidal particles with sizes below 500 nm. These techniques include 'slice-and-view', which is a combination of focused ion-beam irradiation and scanning electron microscopy (SEM) [22], X-ray microscopy [23], and X-ray tomography (either synchrotron [24] or lab-based [25]).

Here, we explore the full 3D real-space structure of supraparticles (SPs) by building on a technique that has previously been used to obtain particle coordinates of particles smaller than 500 nm [26, 27]. In their work, Willig et al. only analyzed three particle layers [27], and it was never followed up on, as far as we know. The technique relies on super-resolution confocal (3D) stimulated emission depletion (STED) microscopy [28, 29], where we first optimized several key parameters to ensure that it can be used for larger crystals. These parameters include the fluorescent core size in core-shell silica colloids [30, 31], SP washing procedure, index matching, and the imaging conditions [32, 33]. After optimization, we were able to analyze 10s of SPs with relative ease, with the acquisition and classification of one SP taking approximately 30 min.

In this paper, we focus on being able to obtain the coordinates of particles assembled into icosahedrally packed SPs within a reasonable time frame. We illustrate this for SPs made from spheres with a diameter below 500 nm, which are especially useful for photonic applications. This is important because it was found that the 3D icosahedral quasicrystalline structure outperformed the best-known photonic crystal lattice, namely the diamond lattice [34]. Similarly, owing to the more spherical arrangement of particles, icosahedrally arranged silica particles were found to outperform SPs with FCC stacking of the same spheres in terms of omnidirectional structural color [17]. Moreover, we compare SP characterization by SEM analysis with quantitative real-space analysis, where we highlight the ability to distinguish onion-shell structures and defects, typically overlooked in surface characterization techniques. We also briefly looked at the final volume fractions of the different types of SPs.

2 | Methods

This section outlines the preparation and measurements of the samples. The particles that were used consisted of fluorescently labeled core-shell particles with core sizes of either 93 or 123 nm, and a total diameter ranging from 442 to 478 nm [30, 31, 35–38]. For smaller core sizes, the fluorescent intensities are so low that longer acquisition times are required, while not necessarily improving the resolution.

For the shells, we found that this was around the minimal shell thickness, where we do not encounter too many problems with the overlap of the fluorescent domains. These particles were then self-assembled using a simplified double-emulsion method as described in Ref. [39]. For a detailed synthesis procedure, see the Supporting Information.

2.1 | Confocal/STED

2.1.1 | Sample Preparation

To enable index matching and analysis without risking structural damage to the SPs due to frictional forces and pressures, house-made microscopy slides were used. These consisted of standard microscopy slides (Menzel GlaÍser) with an 8 mm circular hole drilled into them, where a #1.5H high-precision cover slip (Menzel GlaÍser) was fixed to the bottom with UV-glue (Norland Optical Adhesive 68). The glue was cured with a handheld UV lamp (UVGL-58, 6 watts, 365 nm) for at least 15 min before the samples were prepared. The resulting microscopy slide contained a cylindrical well in which the samples were prepared without risk of damage. For the sample preparation, 20 µL of SP sample (≈0.3 vol% in water) was dropcasted in the cylindrical well and dried at 80°C for 10 min. Given that the SPs are made via vortexing, their sizes range from 5 to 25 µm. This means that some of the particles might still be subject to Brownian motion during the analysis as they redisperse in the index-matching mixture. To eliminate this, 10 µL (1.6 mg/mL) 62 nm silica particles were added to the dried SPs on the glass cover slip and heated for 10 min at 80°C. These particles filled up the remaining free volume between the supraparticle and the bottom cover slip, thereby fixing them in place in the lateral direction. Once the samples had cooled, the cylindrical wells were filled with 100 µL 80% glycerol/water (w/w) immersion liquid. Next, a cover slip (Menzel GlÍaser) was glued to the top with UV glue, sealing off the spherical well. Here, the slight excess volume that is obtained with 100 µL immersion liquid ensures that no air bubbles are trapped inside the wells. The glue was cured for at least 30 min with a handheld UV lamp.

2.1.2 | Confocal (STED) Microscopy

Confocal and STED microscopy measurements were performed using a Leica TCS SP8 3X inverted confocal laser scanning microscope. For our samples, we used a 93x/1.3 HC PL APO CS2 STED objective (Leica #506417) and lens immersion liquid of 80% Glycerol/water (w/w) with a refractive index of 1.4429. From UV–vis absorption measurements, it was determined that the FITC doped in the silica had an absorption maximum at 488 nm. The FITC dyed particles were, therefore, excited using a white-light laser (SuperK) set to 488 nm with an intensity of 3%. The resulting fluorescence was detected on a hybrid detector (HyD) between 498 and 582 nm, with a gating time of 0.3–12 ns. Gating was used to ensure that no reflection signal was captured. The reflection signal was separately captured on a photon multiplier tube (PMT) detector between 478 and 498 nm. Data was acquired in 16-bit depths, and lines were accumulated 4 times to increase the amount of signal per voxel. A scan speed of 200 Hz was used, with image sizes of 512 × 512 px^2 (with typical x,y pixel sizes of 20–50 nm) acquired at a z step size of 80 nm, resulting in typical pixel dwell times of 2.43 µs. Furthermore, a pinhole diameter of 0.7 Airy Units was used to remove out-of-focus light. For STED measurements, a 592 nm continuous wave depletion laser (Leica STED) was used with a typical intensity of 30%, and the 3D STED slider was set to 100% to optimize the resolution in the axial direction. Before each measurement, a STED beam alignment was performed, and the motorized correction collar (motCORR) position was optimized. The motorized correction collar is typically used to correct for varying cover glass thicknesses, which are approximately 5 µm for the #1.5H high-precision cover slip. These variations give rise to deviations in the scattering and spherical aberrations observed when imaging through the glass. The motCORR corrects for these abberations and this has as additional feature that it can also be used to correct for slight refractive index mismatches [40, 41]. The optimization of the motCORR position was done by systematically varying the motCORR, starting with steps of 10%, which were decreased as the ideal position was approached. The quality of the motCORR position was judged by eye by looking at the sharpness of *xz* cross sections, acquired at the image settings used for the data acquisition. As the motCORR position is slightly depth dependent, the position was determined for the regions that were to be scanned over. All measurements were done between 18.8°C and 19.5°C. The reason for this narrow temperature range was to ensure that only small, motCORR compensable fluctuations in refractive index occurred. Larger deviations in refractive-index mismatch cause aberrations, which, in turn, lead to overlap of the fluorescent domains, causing issues with the particle localization. We generally found that refractive-index mismatches of 0.005 were enough to cause particle localization issues.

2.1.3 | Post-Processing

All images were acquired in the Leica Application Suite (LAS) X software (v3.5.6), and processed using Huygens Professional (v23.04, Scientific Volume Imaging). For further processing, the data were stabilized by aligning adjacent z-slices using cross-correlation, Lanczos interpolation, and iterative filtering. After this drift correction, they were deconvolved using the Classic Maximum Likelihood Estimation algorithm. In this algorithm, the automatically assigned signal-to-noise ratio (SNR), automatically assigned background estimation, a maximum of 40 iterations (or until a quality threshold of 0.01 was reached), and an acuity of 13.8 were used. The deconvolution was performed on both the reflection and the fluorescence signals.

2.1.4 | Particle Localization

Particle coordinates were extracted from the post-processed microscopy data using trackpy (v0.6.3) [42], which is based on the particle tracking algorithm of Crocker and Grier [43]. In this localization, the particle diameter was typically set to values between 300 and 400 nm in *xy* and to 550 nm in *z*, with a minimal separation between 300 and 400 nm in all directions. After particle localization, any loose particles that are not part of the SPs were removed.

2.1.5 | Data Analysis

To classify the different local orders within the self-assembled systems, we follow the method presented in Ref. [44]. We first determine the nearest neighbors for each particle i using the solid angle nearest neighbor (SANN) criterion [45], which also provides a nearest neighbor radius, $r_{\mathrm{SANN}}(i)$.

Next, we compute complex bond orientational order parameters, with ℓ ranging from 1 to 12, which for a particle is i defined as [46]:

$$q_l^m(i) = \frac{1}{|\mathcal{N}(i)|} \sum_{j \in \mathcal{N}(i)} Y_l^m(\hat{r}_{ij}) \tag{1}$$

where Y^m are the spherical harmonics, $\hat{r}_{ij}$ is the unit vector from particle i to its neighbor j, and $N(i)$ denotes the set of nearest neighbors of particle i. Following Ref. [47], we then average the bond order parameter locally via:

$$\bar{q}_l^m(i) = \frac{1}{1 + |\mathcal{N}(i)|} \sum_{k \epsilon \{i\} \cup \mathcal{N}(i)} q_l^m(\mathrm{k}) \tag{2}$$

From these complex coefficients, we compute the real rotation-invariant order parameters [47]:

$$\bar{q}_l(i) = \sqrt{\frac{4\pi}{2l+1} \sum_{m=-l}^{l} \left|\bar{q}_l^m(i)\right|^2} \tag{3}$$

To complement these orientational descriptors with a measure of positional symmetry, we first calculate the center of mass of the nearest neighbors:

$$r_{NNC}(i) = \frac{1}{|\mathcal{N}(i)|} \sum_{j \epsilon \mathcal{N}(i)} r_{ij} \tag{4}$$

Then, we normalize the distance between the particle and its NN center by the NN radius:

$$\delta r\left(i\right)=\frac{\left|r_{i}-r_{NNC}\left(i\right)\right|}{r_{SANN}\left(i\right)} \tag{5}$$

This scalar parameter captures deviations from local centrosymmetry and can help distinguish highly ordered environments from asymmetric or interfacial ones.

Together, these descriptors form a 13D feature vector (per particle) that encodes the local structure of each particle.

Then, we feed this data into the pre-trained UMAP and Gaussian mixture models given in Ref. [44] to reduce the dimensionality to 3 and classify particles into 20 clusters. Finally, we use the entropy-based cluster merging [48] to reduce the number of clusters to 12. We note that this is fewer than the number of clusters presented in Ref. [44] since we reduced the number of clusters to account for experimental tracking noise.

2.2 | Particle Size Determination

Intermediate particle sizes were determined using transmission electron microscopy (TEM) images, captured on a Talos L120C microscope with an acceleration voltage of 120 kV. From these images, the particle sizes and polydispersities were determined via an in-house developed Python script. This script is based on a watershed algorithm to which distance transforms and automatic thresholding are applied, before fitting ellipses to each particle. The reason this method has not been applied to the final particle sizes is that beam damage causes the silica particles used here to shrink. This effect is already noticeable, even at minimal exposure times (0.25 s) and dose rates (0.28 e/nm^{2}s) at low magnifications.

Since the final particle sizes are used to calculate the packing fraction, we did not determine the particle sizes from TEM images. All polydispersities were determined from the TEM images, as the shrinkage is consistent per sample.

Instead, the final particle sizes were determined from the particle coordinates obtained from confocal microscopy. For each particle, the distance to its nearest neighbours was calculated. The effect of possible defects or dumbbells was excluded by setting a minimal distance of 0.85x the expected particle size and a maximum distance of 1.05x the expected particle size. Due to pixel biasing during the tracking, small offsets (of around 5 nm) in the coordinates were systematically obtained. The outcome was verified by measuring FCC-like domains that were parallel to the xy-plane to minimize deviations resulting from optical effects in the axial direction. The particle sizes in these FCC-like domains were consistent with what was calculated based on the nearest neighbor distances.

2.2.1 | Packing Fraction Determination

The packing fractions of the SPs were determined using a convex hull-based approach (see SI). Each particle was first represented as an icosphere comprising 642 vertices. From these vertices, a convex hull was generated, corresponding to the smallest volume that fully encloses all particles within the SP. The packing fraction was then calculated as the ratio of the total particle volume to the total volume enclosed by the convex hull.

3 | Results

As described in the experimental methods, SPs were prepared using the simplified double emulsion method developed by Wang et al. [39]. This was done because the flux of water through the oil layer, and thus the self-assembly speed, can be controlled using the osmotic pressure of the dispersion liquid [13, 49].

Since these emulsions were made through vortexing, a variety of SP sizes (5–30 µm) were found and could be investigated for one set of drying conditions. Within this size regime, the supraparticles consist of around 2000 to nearly 200 000 particles. As a result, the smaller supraparticles tend to reach equilibrium and exhibit a higher degree of overall icosahedral yield, while the larger supraparticles tend to be slightly out of equilibrium.

We began our analysis using the most conventional technique: scanning electron microscopy (SEM). Although SEM has the advantage that a large number of SPs can be analyzed relatively quickly and easily, it provides no information about the internal structure of the SPs. As a result, in past literature, SPs that have a disordered outer shell have been commonly classified as either disordered, spherical, or partially ordered [8, 50]. Here, we quantitatively analyzed the SPs using SEM based on their surface features. We categorized the SPs into three categories: crystalline, partially crystalline, and disordered.

Specifically, SPs that consisted of fully truncated triangular and rectangular domains with icosahedral symmetry were classified as crystalline. If truncated triangular and rectangular domains were present in combination with hexagonally or disordered domains, it was classified as partially crystalline, and if it consisted almost exclusively of hexagonally or disordered domains, it was classified as disordered. The results are summarized in Table 1.

In addition to the SEM, we also categorized the same sample of SPs (meaning SPs from the same sample, but not the same SPs themselves) using confocal/STED microscopy. This allowed us to also examine the interior of the SPs. This structure determination was based on 20 central z-slices of the internal structure, to allow for the analysis of over a hundred SPs within 2 h. The results of this analysis are also shown in Table 1.

We now compare the SEM and confocal/STED results. As a first observation, we see that the fraction of disordered SPs in SEM corresponds closely to the fraction of onion-shell SPs that was observed with confocal/STED. Additionally, there is a noticeable difference between the number of partially crystalline and fully crystalline SPs between the two techniques. There are two reasons why confocal/STED gives an apparently higher crystalline yield. First, in STED, we only analyze the central part of the SPs. Disordered domains are typically located at one side of the SP and might be missed here. As such, quantitative analysis in this way is prone to overestimation of the crystalline yield. Second,

TABLE 1 | Quantitative analysis results from both scanning electron microscopy and confocal/STED microscopy. With SEM, the particles were classified as disordered, whereas confocal/STED revealed that these were onion-shell structures.

Analysis technique	SPs analyzed	Crystalline (%)	Partially crystalline (%)	Disordered/Onion-shell (%)
SEM	197	54	36	10
Confocal/STED	110	64	28	8

structures, without clear faceting, that contained a partial single concentrically ordered layer are difficult to distinguish from fully crystalline structures. As such, both were classified as fully crystalline SPs, whereas the former might appear as partially crystalline in SEM.

To further examine the structure, we extracted all the particle coordinates for 22 SPs using confocal/STED microscopy. All of these supraparticles are provided as Supporting Information and can be visualized in HTML5-compatible browsers. In these supporting files, the supraparticles can be rotated (click and drag), sliced along the viewing direction to make cross-sections (top slider), and radially sliced to visualize the different layers (bottom slider). We have also added ideal icosahedral and ideal decahedral supraparticles for comparison. These were then fully characterized and analyzed via an unsupervised machine learning algorithm as described in Ref. [44]. In contrast to Ref. [44], where 16 distinct local particle environments were identified, the algorithm was here adapted to classify 12 broader environments to reduce the influence of positional noise in the tracked particle coordinates.

A much richer set of structures was found than can normally be observed from SEM data. Additionally, due to the larger number of analyzed SPs, this also provides more information than the few SPs that have been examined using other real-space techniques in the past [17, 19]. In the following, several illustrative structures will be discussed, including surface-reconstructed icosahedral SPs, onion-shell SPs, where the inside is ordered, but the outer layers form concentric rings, defective icosahedral clusters, and decahedral SPs. For comparison, we have also added magic number icosahedral and decahedral supraparticles, which are generated with distorted FCC building blocks that maximize packing and symmetry [8]. We note that, while this might be comparable to what is obtained from experimental systems, these structures might not be equilibrium SPs. The magic number terminology comes from the fact that these supraparticles form closed-shell structures. Experimentally, it is unlikely to obtain a structure with an exact magic number. Instead, supraparticles typically contain slightly more or slightly fewer particles.

Under spherical confinement, such deviations lead to the formation of alternative, more defective structures, as also observed by Wang et al. [19].

3.1 | Icosahedral Structures

Among the SPs discussed here, icosahedral SPs have been studied the most extensively in literature [3, 4, 6, 8, 12, 17, 50, 51]. In Figure 1A, we show a SEM image of such an icosahedral SP, which shows all the distinct surface features associated with an anti-Mackay cluster. Namely, the truncated triangles that alternate with truncated rectangles around fivefold axes, which are decorated with several concentric rings [7–10]. Looking at the cross-section of the ideal SP (Figure 1G), we can also see the individual Mackay (triangular domains pointing radially inward) and anti-Mackay tetrahedra (isosceles trapezoids pointing radially outward on top of each triangular domain).

The anti-Mackay tetrahedra are also visible in the radial slice in Figure 1B, where the outer layer is removed. This was done to better visualize the machine learned and classified clusters, as the surface contains fewer nearest neighbors, leading bond-order analysis to classify the surface as a single class [44].

These anti-Mackay faces can now be identified as the truncated triangles on the surface of this radially sliced cluster. By slicing additional layers, the entire surface reconstructed shell can be removed, as shown in Figure 1C. Here, the transition between the anti-Mackay and the Mackay tetrahedra is visible. This transition contains an edge, as expected, between two slightly deformed FCC domains. One layer deeper in the crystal, we reach the Mackay tetrahedral domain, as shown in Figure 1D. In this case, the Mackay tetrahedra point inward, whereas the anti-Mackay tetrahedra point outward. For this same SP, we also examined a cross-section, shown in Figure 1E, where the previously discussed features can be observed as well. The interior consists of Mackay tetrahedra that converge toward the center of the SP. On the outside, several anti-Mackay tetrahedra can be seen, but they are present only in two of the six planes. This could indicate that the crystallization rate might have been slightly too fast for complete surface reconstruction to occur.

Another noticeable feature that is visible in the cross-section in Figure 1E is that there is a defect line that runs throughout the entire cross-section. This defect line is relatively narrow on the right, but becomes progressively broader toward the left-hand side. Wang et al. [19] simulated what happens when the total number of particles deviates from the nearest magic number structure and found that this can lead to several different structures forming. There can be an accumulation of defects in one or multiple tetrahedra, or there can be a formation of a so-called wedge defect, which is what we observe here. Indeed, if we compare the number of tracked particles to those in the magic number clusters identified by Wang et al. [8], we see that we have 208 particles fewer than the nearest magic number structure. This structure has 14 Mackay layers and 4 anti-Mackay layers, which is indeed what we observe for the surface reconstructed domains of this SP.

A similar cross-section was obtained for a smaller SP (Figure 1F) containing about a third of the number of particles. For this

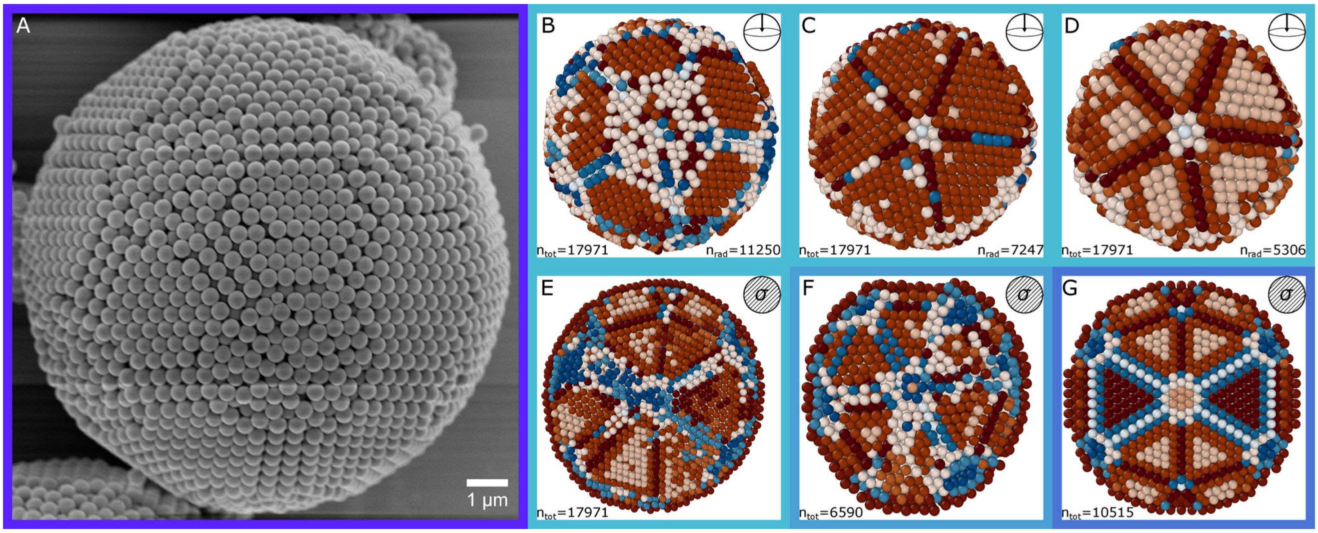

FIGURE 1 | (A) SEM visualization of a surface-reconstructed icosahedral SP. (B–G) Particle coordinates were classified using a machine-learning-based bond-order parameter analysis and are color-coded according to the different symmetry classes. The SPs are shown using two methods, which are illustrated in the top right corner. For radial slices (B–D), depicted by ⊕, we removed particles layer by layer starting from the outside. For this specific visualization, we give both the total number of particles (n_{tot} bottom left) and the number of particles remaining in the visualization (n_{rad} bottomright). For cross-sections (E–G), depicted by (σ), we take a slice through the center of the SP. (B) Radial slice revealing the anti-Mackay tetrahedra on the outer surface of the SP, with only the outermost layer removed. (C) Radial slice after removal of the anti-Mackay tetrahedra (outer 3 layers), highlighting the transition between Mackay and anti-Mackay tetrahedra. (D) Radial slice one layer deeper, where only Mackay tetrahedra remain. (E) Cross-section through the center of the SP shown in (B–D), visualizing the threefold symmetry axis and revealing anti-Mackay tetrahedra in three of the six regions. (F) Cross-section through a different SP along the threefold axis, showing the arrangement of Mackay and anti- Mackay tetrahedra in all directions, which aligns well with the expected magic-number icosahedral structure. (G) Magic number icosahedral structure with particle coordinates modeled and given by Wang et al. [8], serving as a comparison for the experimental results.

SP, no wedge defects were found, and the anti-Mackay structure is visible around most of the SP. Interestingly, the Mackay tetrahedra are not equally well defined everywhere.

Some appear more disordered than the others. This could be explained by some tetrahedra having more time to fully crystallize and reorder before twinning. This is in agreement with predictions from simulations, which suggested that the tetrahedra grow independently [6, 12]. Another feature that can be seen in this SP is that an accumulation of disorder can be observed near the surface at the five-fold axes. The migration of defects to these positions is likely driven by the lower lattice strain near the surface at the five-fold axes, similarly to how large particles tend to migrate to these positions as well [52]. Like the previous SP, this SP was also compared to the closest magic number structure, which contains 9 Mackay layers, 4 anti-Mackay layers, and a total of 6861 particles. Indeed, 9 Mackay layers are observed, but only 3 anti-Mackay layers are present. This discrepancy is likely because the experimental SP contains 271 fewer particles than the magic number cluster.

Moreover, we also compared the structures of both experimental SPs to that of a magic number icosahedral SP, shown in Figure 1G [8]. If we compare the Mackay tetrahedra of the experimental SPs to those of a magic number cluster, we see that the general features look quite similar. This is specifically noticeable for the general symmetry of the small SP shown in Figure 1F. The experimental systems are dried, which leads to a general increase in the packing fraction and an appearance that is generally slightly closer to FCC-like structures. This is an indication that these magic number clusters are likely no longer equilibrium structures.

3.2 | "Onion-Shell"-Type Supraparticles

Another type of particle that we were able to observe in detail using STED/confocal microscopy was the onion-shell structure, as shown in Figure 2. That we are able to characterize onion-shell structures clearly demonstrates the importance of quantitative real-space analysis, as this is a structure that requires information about the inside of the SP. Figure 2A,D shows the exterior of two different SPs that appear disordered. If quantitative measurements were conducted using SEM, these SPs would be classified as either partially ordered or disordered, depending on their orientation [50]. However, when additional layers are radially removed, the same Mackay icosahedral structure, as normally found in fully crystalline SPs, is observed. We illustrate this in Figure 2B by radially removing four additional layers of the first SP. This indicates that the SP actually possesses a lot of order and is likely to exhibit photonic properties similar to those of anti-Mackay SPs. This similarity arises because the vast majority of the ordered structure, which determines its photonic properties, remains icosahedral.

For both SPs, we also show the cross-sections. In the larger SP, shown in Figure 2C, an anti-Mackay tetrahedron is visible in the extension of the upper Mackay tetrahedron, indicating that the drying rate allowed for some surface reconstruction, but was too fast to form a fully anti-Mackay structure.

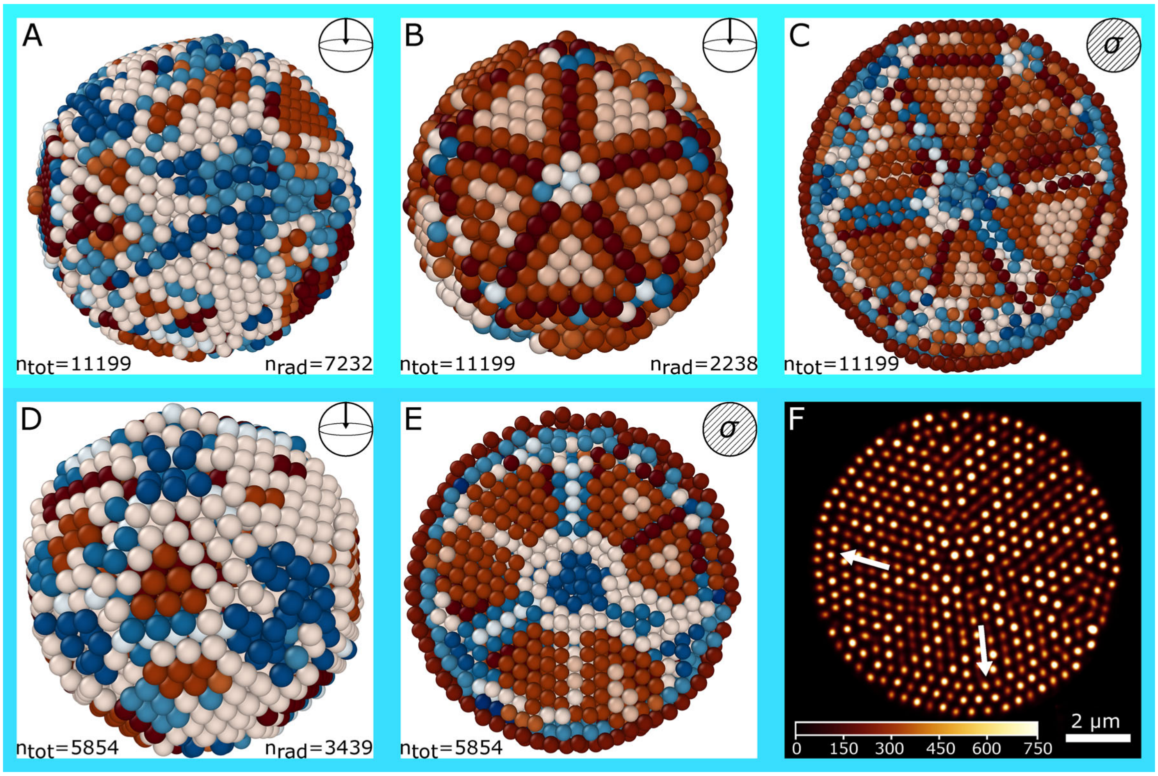

FIGURE 2 | Visualization of an onion-shell type SP. (A) Radial slice 2 layers deep in the SP, showing the disordered structure exterior. (B) Radial slice 6 layers deep within the SP, revealing clear icosahedral symmetry. (C) Cross-section of the SP shown in (A) and (B), taken along the threefold axis, illustrating the internal icosahedral symmetry and a disordered outer structure in four of the six symmetry directions. (D) Radial slice of a smaller SP, highlighting its disordered outer structure. (E) Cross-section of the SP shown in (D), taken along the threefold axis, showing an internally ordered SP with concentric rings in the outer 2–3 layers. (F) Confocal slice of the SP shown in (D) and (E), taken along the threefold axis, where the outer layer(s) deviate from the underlying crystal structure.

For the smaller SP, shown in Figure 2E, no surface reconstruction is observed. Instead, two complete concentric shells enclose the ordered interior. These concentric shells are also visible in the confocal slice shown in Figure 2F, where the SP happened to be lying in an orientation that allowed for the acquisition of slices along the threefold axis. In this figure, the transition between the Mackay tetrahedra and the concentric shells is indicated by arrows, highlighting local variations in the number of concentric shells.

3.3 | Defective Supraparticles

Another important property of the SPs that can now be classified in much more detail is the defects that occur in the SA, enabling us to examine their influence on the optical properties in future work. An example of defects was already shown in Figure 1E,F, where wedge defects and disorder in some of the Mackay tetrahedra were observed, respectively. In the following, we discuss two additional examples, featuring different types of defects that can be observed from real-space analysis, but are not apparent from the external structure.

For most icosahedral SPs, the Mackay tetrahedra are found to be symmetrically organized around the center of the SP in both experiments and simulations. However, this is not the case for the SP shown in Figure 3A–C. In the radial slice in Figure 3A, the three Mackay tetrahedra on the right appear larger than the two Mackay tetrahedra on the left. Without analyzing the full structure, it is difficult to determine whether this is merely a surface feature or if it affects the entire SP structure. However, when examining the cross-section in Figure 3B, we observe that the symmetry point is not centralized, a finding that is further supported by the confocal slice in Figure 3C. One possible explanation is that some of the tetrahedra were slightly larger prior to twinning. If the growth of one or several of the tetrahedra starts earlier than the others, it could result in an off-center symmetry point. The resulting structure is most likely out of equilibrium, but locked in due to kinetic effects. The independent growth of the tetrahedra is in agreement with previous simulations of the SP nucleation and growth in previous simulations of SP nucleation and growth [6, 12]. A notable difference in the SP shown in (Figure 3A) is that the Mackay tetrahedra extend to the surface, with no anti-Mackay structure and barely any concentric shells. The off-centered symmetry point could cause the transition between Mackay and anti-Mackay structures to become ill-defined. If anti-Mackay tetrahedra were to form, they would adopt an equally large tetrahedral basis as the underlying Mackay tetrahedra. Since these 20 tetrahedra differ in size, the space between them cannot be filled in the same fashion as for more symmetric anti-Mackay tetrahedra. This likely makes surface reconstruction less favorable, leading to an adaptation of the underlying Mackay tetrahedra's geometry to minimize the free-energy penalty in spherical confinement.

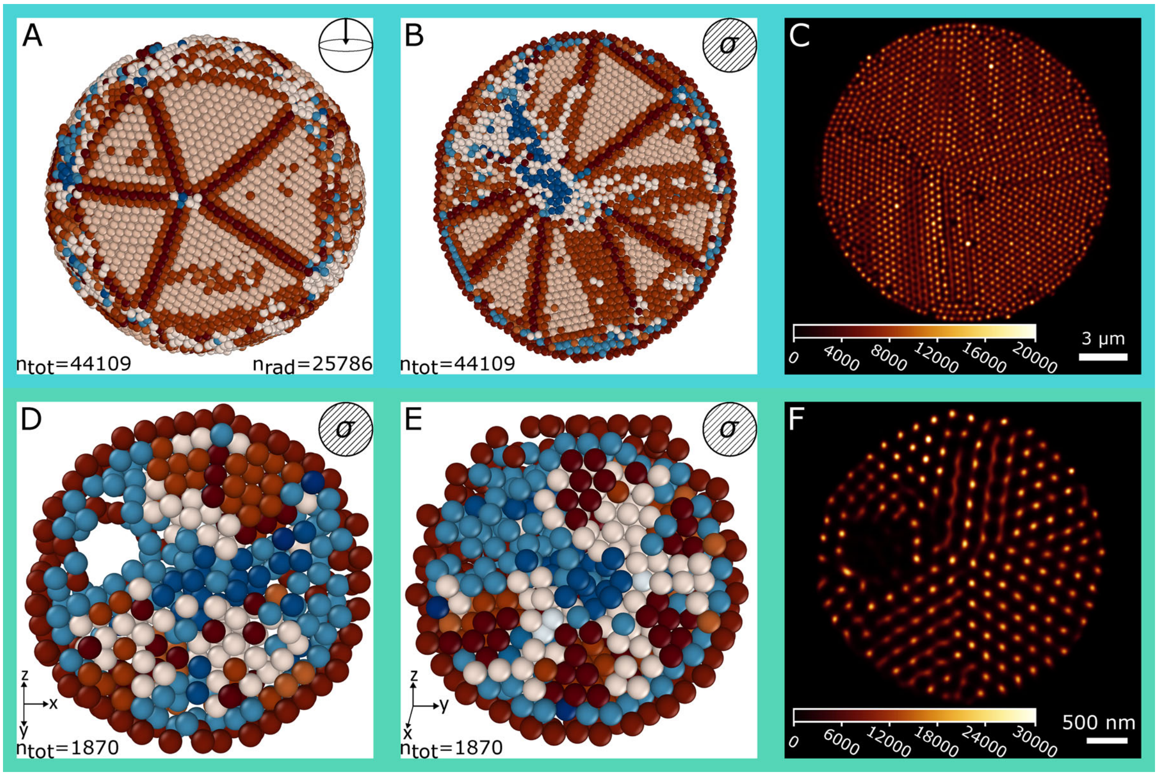

FIGURE 3 | Visualization of defective icosahedral SP structures, highlighting two types of defects that are not visible from the external structure. (A) Radial slice of the outer structure of an icosahedral SP, revealing Mackay tetrahedra. Some tetrahedra appear larger than others, indicative of an off-center symmetry point. (B) Cross-section of the same SP shown in (A), demonstrating that the convergence point of the Mackay tetrahedra is not centralized within the SP, deviating from the typical icosahedral symmetry. (C) Confocal slice of the same SP shown in (A) and (B), where the off-centered symmetry point and the surrounding Mackay tetrahedra are shown as well. (D) Cross-section of three colloidal layers within an SP, revealing a large structural defect. (E) Cross-section of the same SP, but now rotated to indicate the limited effect of the structural defect on the overall structure. (F) Confocal slice of the same SP shown in (D), but now in the middle of a structural defect.

Another type of defect that cannot be detected by examining the surface of the SPs is point defects or spherical inclusions. In Figure 3D, we show three layers of an SP that reveal a hole in the structure. This hole likely resulted from a stabilized oil droplet in the water phase, forming a w/o/w/o emulsion.

During the drying process, this oil droplet became trapped within the structure, creating the observed defect. This particular defect has a diameter of approximately 1.2 µm, equivalent to three particles lying side-by-side, indicating that it is unlikely to have originated from the particles used in the self-assembly. Interestingly, this defect appears to have had only a limited effect on the icosahedral structure of the SP. In the plane containing the defect, two of the six expected Mackay tetrahedra are clearly visible, and the icosahedral structure becomes even more apparent when a cross-section is taken after rotating around the z-axis, as shown in Figure 3E. This orientation shows similarities to the SPs shown in Figure 1. The exception is that for this defective SP, no anti-Mackay structure is observed. The number of particles in this structure, 1870, is relatively close to the magic number for an SP with eight Mackay and zero anti- Mackay layers, which has 1863 particles. As such, it is unsurprising that no anti-Mackay or onion-shell structures are visible in this SP, which indeed contains around Mackay layers.

3.4 | Decahedral Supraparticles

Decahedral SPs are typically found at low concentrations in self-assemblies with high yields of anti-Mackay clusters [11, 12]. Theoretically, the maximum yield of decahedral SPs is 13% [12], and under experimentally optimized conditions with a large number of particles and fast drying rates, up to 10% can be obtained [11]. The symmetry of these clusters is significantly lower than that of icosahedral SPs. The most recognizable feature is that there is only one fivefold symmetry axis running through the middle of the SP. These clusters consist of five domains that converge along the central fivefold axis, as clearly shown in the ideal decahedral in Figure 4D. As with icosahedral SPs, the five faces arranged around the fivefold axis consist of truncated triangles, indicating an {111} FCC-like plane (Figure 4E). Along the equator, the central plane perpendicular to the five-fold axis, the particles are arranged in a square particle geometry, characteristic of an {100} FCC-like plane, which can be seen most clearly in the side-view provided in Figure 4G.

Here, we performed a real-space analysis on a decahedral cluster and compared it to the magic number decahedral cluster described in Ref. [12]. Our results are summarized in Figure 4A–C,G. For the experimental cluster, the decahedral

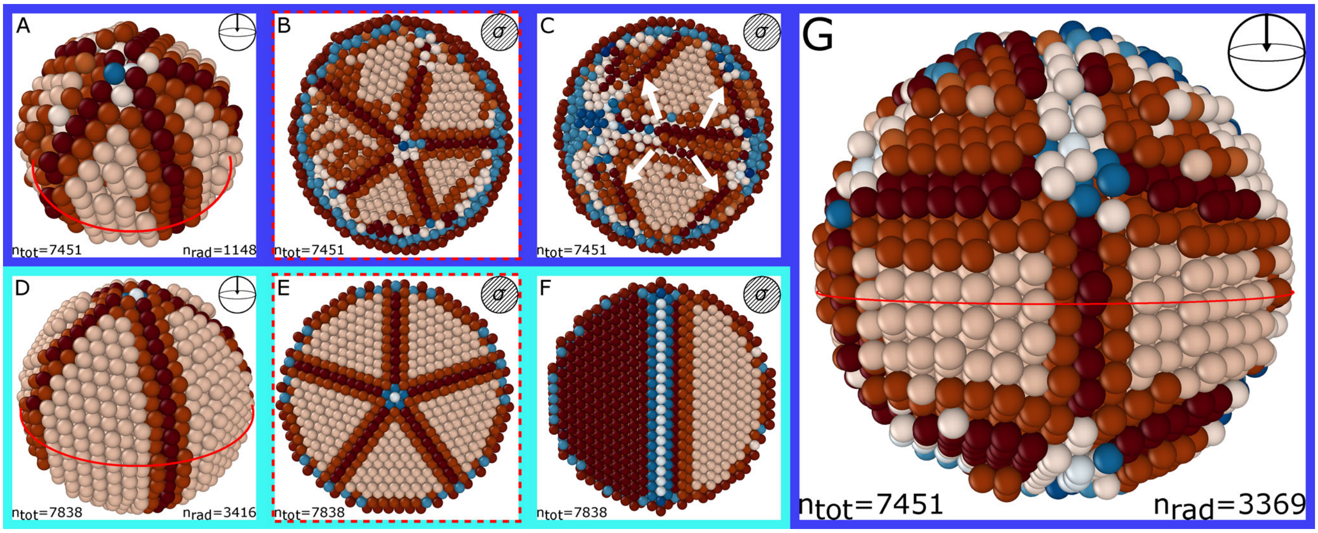

FIGURE 4 | Visualization and comparison of an experimental (A, B, C, G) and a magic number (D–F) decahedral SP, for which the coordinates were obtained from [12]. In the radially sliced panels (A, D, G), the equator, the central plane perpendicular to the fivefold axis, is indicated by a red line. (A) Radial slice of an experimental decahedral SP. (B) Cross-section along the equator, indicating that the five-fold axis runs throughout the entire SPs. (C) Cross-section along one of the domain edges, where the arrows indicate the places where surface reconstruction on the {111} planes occurs. (D–F) The same slices but now acquired for a magic number decahedral SP of approximately the same size. (G) Radial slice of the experimental decahedral SP, showcasing the anti-Mackay features on top of the {111} planes and the additional five-fold symmetry that becomes apparent on the surface of the SP.

structure becomes evident after radially removing seven layers, as shown in Figure 4A. This structure closely resembles the magic number decahedral cluster in Figure 4D. From this radial slice, we can clearly see the central fivefold axis running through the SP. We also examined a cross-section along the equator for this SP, shown in Figure 4B, which also resembles the cross-section of the magic number cluster, shown in Figure 4D. The fivefold symmetry is preserved throughout the entire structure, as expected for decahedral SPs. One notable difference is that the fivefold symmetry axis is slightly below the center of the SP. This off-centered decahedral symmetry has been reported in literature more often [11, 25, 53] and is suggested to have the same origin as the off-centered icosahedral SPs, where some tetrahedra grow slightly faster than others [12]. Furthermore, we analyzed a cross-section along one of the domain edges and observed a distinction between the experimental and magic number SP structures. The experimental SP, in Figure 4C, exhibits additional tetrahedra edges near the surface. These edges are small, and little order is present. We investigated whether this was related to the off-centered fivefold axis, but these features were found in all five domains. These edges bear some resemblance to the transition between Mackay and anti-Mackay tetrahedra, suggesting that the experimental structure may be undergoing a similar surface reconstruction to maximize its entropy. However, based on our observations, surface reconstruction in this decahedral SP appears to be confined to the {111}- like planes and was not observed on the {100}-like planes. This is likely due to surface reconstruction being more favorable on {111}-like planes than on {100}-like planes. The surface reconstruction is more clearly visualized in the radial slice in Figure 4G, where it can be seen on all {111}-like planes. Additionally, the presence of these anti-Mackay tetrahedra introduces more fivefold symmetry points at the surface. As a result, it is no longer straightforward to accurately characterize this decahedral SP based solely on surface features. Whether this phenomenon occurs more frequently in decahedral SPs remains unclear, as not enough of these particles were investigated at this stage. However, this finding may provide another explanation for why these structures are so rarely found in some samples, specifically in studies targeting clusters where no magic-number icosahedral structures are nearby. Finally, these findings are yet another example of the importance of quantitative 3D real-space analysis, as it remains the only method capable of accurately determining the underlying decahedral structure and collecting statistical data on these clusters.

3.5 | Packing Fractions

To further characterize the SPs, we measured their packing fractions. The packing fraction of an SP depends on the definition of the confining geometry. In this case, we defined the packing fraction as the fraction of the volume inside the convex hull that surrounds the SP occupied by particles.

We begin our analysis by looking at a few idealized cases, which will act as benchmarks for our experimental SPs. We start by looking at the smallest clusters consisting of a particle with a single shell around it (in total, this cluster has 13 particles). Consistent with the literature, we find that for an FCC arrangement of particles, we have the highest packing fraction: 64.98%. An icosahedral arrangement leads to a lower packing fraction of 63.47%. We then examined a wide range of "cookie-cutter" FCC clusters, where a spherical cluster is cut out of a bulk FCC crystal. The results are shown in Figure 5, and specifics for the individual SPs are given in the SI, but we generally find that the packing fraction increases slowly, not even reaching the bulk limit for five million particles (where it hits 73.34%). We similarly looked at the best packing of magic number icosahedral SPs, finding it stays below the FCC results by around 2%.

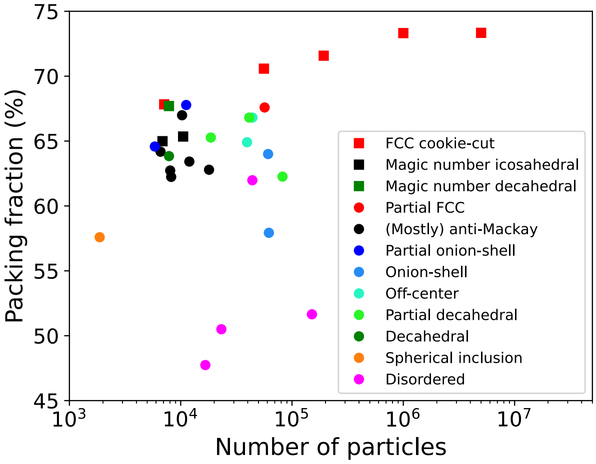

FIGURE 5 | Packing fractions of cookie-cut FCC clusters, magic number clusters, and experimentally analyzed SPs.

Interestingly, we also examine the packing fraction of the magic number decahedral SP and found that it is significantly higher than the magic number icosahedral SP, and approaches closely that of the FCC cluster.

On the experimental side, the smallest SP that we analyzed (excluding the SP with the hole) contained 5854 particles, and is the (partial) onion-shell SP shown in Figure 2D,E. This particular SP had a packing fraction of 64.58% and contained no defective Mackay tetrahedra. We also analyzed some other SPs with fewer than 10 000 particles, which contained defects in one or more of the tetrahedral domains. The first SP, containing 6590 particles, contains one defective Mackay tetrahedron, off-axis to what is shown in Figure 1F. This SP has a packing fraction of 64.18%, indicating that the defective structure causes a slight decrease in the packing fraction. To study the effect of more defects, we also analyzed an SP with 8047 particles, and 2–3 defective Mackay tetrahedra, which has a packing fraction of 62.73%.

This supports our finding that the packing fraction decreases with more defective structures, even if the number of particles increases.

If we now look at slightly bigger SPs in Figure 5, we observe that some experimental SPs actually have a higher packing fraction than what was observed for the magic number cluster with a similar number of particles. Both a partial onion-shell SP with 11199 particles (67.78%) and a mostly anti-Mackay SP with 10286 (66.99%) have a higher packing fraction. Both of these SPs have a high degree of icosahedral order and contain a single wedge defect. One likely reason they appear higher is that they contain fewer anti-Mackay layers. The anti-Mackays layers tend to pack less efficiently because there are more particles outside the distorted FCC (anti-Mackay tetrahedra), causing the overall packing to be lowered. Both experimental systems contained (locally) at most 3 anti-Mackay layers, but generally fewer, as they were also slightly egg-shaped. This allowed them to adopt fewer anti-Mackay layers along the minor axis. Whether the egg shape was a result of maximizing the packing is unclear.

At even larger particle sizes, we found fewer anti-Mackay structures, but more off-center structures, likely because of drying rates used in the self-assembly. Due to the independent-growth mechanism of the tetrahedra, some tend to be larger, and if not enough time is available for reorganization, these structures lock in due to kinetic effects. We note that these structures are likely not equilibrium structures and are mostly the result of kinetics. As these off-center SPs were typically found with little to no surface reconstruction, it is not that strange that these structures also appeared with higher packing fractions. Approaching even larger clusters, we also found a SP that exhibited more FCC properties, and unsurprisingly, this also has a relatively high packing fraction (67.58%). Finally, we note that structures that only have some ordered domains tend to have a lower packing fraction, and that the most disordered SPs were found to have the lowest packing fraction.

4 | Conclusion

In summary, we have successfully studied a variety of SPs using quantitative confocal/STED microscopy on fluorescent core-shell silica particles < 500 nm in diameter. The analysis through bond-order parameters using a UMAP-based machine-learning algorithm proved to be a good way of identifying icosahedral symmetry within these experimental datasets. From the analysis of the icosahedral structures, we are able to confirm that the tetrahedra grow individually. The presence of defects in some tetrahedra, but not in others, is an indication that the Mackay tetrahedra grow independently from each other. We also found confirmation of the formation of wedge-defects when the number of particles in the SP deviates from close-shell structures. When the SPs exhibit (wedge-)defects, we found that the packing fraction generally decreases. Structures with barely any defects were found to come close to the packing fraction of the magic number clusters, while supraparticles with fewer anti-Mackay layers were found to yield even higher packing fractions. Here, we also demonstrated the ability to classify the onion-shell structures from full 3D data. This enables more precise classification than is available for currently used surface-based analysis techniques. As demonstrated here, the surface does not always represent the underlying structure. Moreover, we found strong indications that concentrically ordered shells first crystallize at the outside of the SPs, and that these later reorder to form anti-Mackay structures to minimize their free energy. Too fast drying rates prevent this surface reconstruction from fully happening, resulting in the formation of onion-shell structures.

Additionally, we found that spherical inclusions formed by "droplet-in-droplet" systems did not affect the ordering of the structure where these droplets got trapped. We also found new evidence regarding the elusive nature of the decahedral SPs. Namely, we found first indications that these can also possess surface reconstructions, making it more difficult to accurately characterize these with commonly used surface analysis techniques. Clearly, our results for these supraparticles indicate that this method is easily generalizable to other colloidal structures self-assembled from photonically relevant particles with diameters less than 500 nm. In future work, it will be interesting to be able calculate the photonic properties of the analyzed structures and compare these to experimental measurements.

Author Contributions

J.I.B., L.D.H., R.Y., and A.v.B. contributed to project conceptualization and design of experiments. A.U. and L.F. contributed to the machine-learning model conceptualization. A.U. trained and provided the classifier and convex hull implementation. J.I.B., L.D.H., and R.Y. performed synthesis of core-shell particles, self-assemblies, and confocal data analysis. J.I.B. performed the quantitative analysis and fully characterized the SPs. J.I.B., L.D.H, and A.v.B. wrote the initial manuscript. All authors reviewed and edited the manuscript.

Acknowledgements

We thank Maarten Bransen for the initial work he did in fixing the SPs and for developing the Python script for determining particle sizes and tracking. This work was done as part of the Advanced Research Center Chemical Building Blocks Consortium, ARC CBBC, which is cofounded and cofinanced by the Dutch Research Council (NWO) and the Netherlands Ministry of Economic Affairs and Climate Policy. AU, RY, AvB, and LF acknowledge funding from the Dutch Research Council (NWO) under the grant number OCENW.GROOT.2019.071. L.D.H. and A.v.B acknowledges funding from the Netherlands Center for Multiscale Catalytic Energy Conversion (MCEC), an NWO Gravitation programme funded by the Ministry of Education, Culture and Science of the government of the Netherlands.

Conflicts of Interest

The authors declare no conflicts of interest.

Data Availability Statement

All tracked data has been uploaded and can be reviewed in the HTML files. Any other data will be shared upon reasonable request.

References

1. T. Hales, M. Adams, G. Bauer, et al., “A Formal Proof of the Kepler Conjecture,” *Forum of Mathematics, Pi* 5 (2017): 2, https://doi.org/10.1017/fmp.2017.1.

2. S. Torquato and F. H. Stillinger, “Jammed Hard-Particle Packings: from Kepler to Bernal and Beyond,” *Reviews of Modern Physics* 82, no. 3 (2010): 2633–2672, https://doi.org/10.1103/RevModPhys.82.2633.

3. D. R. Nelson and F. Spaepen, “Polytetrahedral Order in Condensed Matter,” *Solid State Physics* 42 (1989): 1–90, https://doi.org/10.1016/S0081-1947(08)60079-X.

4. V. N. Manoharan, M. T. Elsesser, and D. J. Pine, “Dense Packing and Symmetry in Small Clusters of Microspheres,” *Science* 301, no. 5632 (2003): 483–487, https://doi.org/10.1126/science.1086189.

5. E. Lauga and M. P. Brenner, “Evaporation-Driven Assembly of Colloidal Particles,” *Physical Review Letters* 93, no. 23 (2004): 238301, https://doi.org/10.1103/PhysRevLett.93.238301.

6. B. de Nijs, S. Dussi, F. Smallenburg, et al., “Entropy-Driven Formation of Large Icosahedral Colloidal Clusters by Spherical Confinement,” *Nature materials* 14, no. 1 (2015): 56–60, https://doi.org/10.1038/nmat4072.

7. K. H. Kuo, “Mackay, Anti-Mackay, Double-Mackay, Pseudo-Mackay, and Related Icosahedral Shell Clusters,” *Structural Chemistry* 13 (2002): 221–230, https://doi.org/10.1023/A:1015847520094.

8. J. Wang, C. F. Mbah, T. Przybilla, et al., “Magic Number Colloidal Clusters as Minimum Free Energy Structures,” *Nature Communications* 9, no. 1 (2018): 5259, https://doi.org/10.1038/s41467-018-07600-4.

9. J. Wang, et al., “Breakdown of Magic Numbers in Spherical Confinement,” *ACS Nano* 19 (2025): 11702–11711, https://doi.org/10.1021/acsnano.4c11099.

10. A. L. Mackay, “A Dense Non-Crystallographic Packing of Equal Spheres,” *Acta Crystallographica* 15, no. 9 (1962): 916–918, https://doi.org/10.1107/S0365110x6200239X.

11. R. Ohnuki, Y. Takeoka, and S. Yoshioka, “Structural and Optical Characterization of Decahedral- Type Spherical Colloidal Clusters,” *Chemistry of Materials* 36, no. 6 (2024): 2953–2962, https://doi.org/10.1021/acs.chemmater.3c03306.

12. C. F. Mbah, J. Wang, S. Englisch, et al., “Early-Stage Bifurcation of Crystallization in a Sphere,” *Nature Communications* 14, no. 1 (2023): 5299, https://doi.org/10.1038/s41467-023-41001-6.

13. S.-H. Kim, J.-G. Park, T. M. Choi, V. N. Manoharan, and D. A. Weitz, “Osmotic-Pressure-Controlled Concentration of Colloidal Particles in Thin-Shelled Capsules,” *Nature Communications* 5, no. 1 (2014): 3068, https://doi.org/10.1038/ncomms4068.

14. C. Wu, Q. Fan, and Y. Yin, “Emulsion-Confined Self-Assembly of Colloidal Nanoparticles into 3D Superstructures,” *Cell Reports Physical Science* 3, no. 12 (2022): 101162, https://doi.org/10.1016/j.xcrp.2022.101162.

15. U. Sultan, A. Götz, C. Schlumberger, et al., “From Meso to Macro: Controlling Hierarchical Porosity in Supraparticle Powders,” *Small* 19, no. 27 (2023): 2300241, https://doi.org/10.1002/smll.202300241.

16. S. Wintzheimer, J. Reichstein, P. Groppe, et al., “Supraparticles for Sustainability,” *Advanced Functional Materials* 31, no. 11 (2021): 2011089, https://doi.org/10.1002/adfm.202011089.

17. C. Kim, K. Jung, J. I. W. Yu, et al., “Controlled Assembly of Icosahedral Colloidal Clusters for Structural Coloration,” *Chemistry of Materials* 32, no. 22 (2020): 9704–9712, https://doi.org/10.1021/acs.chemmater.0c03391.

18. F. Montanarella, D. Urbonas, L. Chadwick, et al., “Lasing Supraparticles Self-Assembled from Nanocrystals,” *ACS Nano* 12, no. 12 (2018): 12788–12794, https://doi.org/10.1021/acsnano.8b07896.

19. J. Wang, C. F. Mbah, T. Przybilla, et al., “Free Energy Landscape of Colloidal Clusters in Spherical Confinement,” *ACS Nano* 13, no. 8 (2019): 9005–9015.

20. D. A. Wang, T. Dasgupta, E. B. van der Wee, et al., “Binary Icosahedral Clusters of Hard Spheres in Spherical Confinement,” *Nature Physics* 17, no. 1 (2021): 128–134, https://doi.org/10.1038/s41567-020-1003-9.

21. E. Vlasov, A. Skorikov, A. Sánchez-Iglesias, L. M. Liz-Marzán, J. Verbeeck, and S. Bals, “Secondary Electron Induced Current in Scanning Transmission Electron Microscopy: an Alternative Way To Visualize the Morphology of Nanoparticles,” *ACS Materials Letters* 5, no. 7 (2023): 1916–1921, https://doi.org/10.1021/acsmaterialslett.3c00323.

22. J. E. S. van der Hoeven, E. B. van der Wee, D. A. M. de Winter, et al., “Bridging the Gap: 3D Real-Space Characterization of Colloidal Assemblies via FIB-SEM Tomography,” *Nanoscale* 11, no. 12 (2019): 5304–5316, https://doi.org/10.1039/C8NR09753D.

23. H. W. Nho, Y. Kalegowda, H.-J. Shin, and T. H. Yoon, “Nanoscale Characterization of Local Structures and Defects in Photonic Crystals Using Synchrotron- Based Transmission Soft X-Ray Microscopy,” *Scientific Reports* 6, no. 1 (2016): 24488, https://doi.org/10.1038/srep24488.

24. J. Hilhorst, M. M. van Schooneveld, J. Wang, et al., “Three-Dimensional Structure and Defects in Colloidal Photonic Crystals Revealed by Tomographic Scanning Transmission X-Ray Microscopy,” *Langmuir* 28, no. 7 (2012): 3614–3620, https://doi.org/10.1021/la204580y.

25. S. Englisch, J. Wang, L. J. Roemling, et al., “Crystal Structure and Defect Analysis of Colloidal Supraparticles by Lab-Based X-ray Microscopy,” *Microscopy and Microanalysis* 28, no. S1 (2022): 306–309, https://doi.org/10.1017/S1431927622002008.

26. S. W. Hell, “Far-Field Optical Nanoscopy,” *Science* 316, no. 5828 (2007): 1137395, https://doi.org/10.1126/science.

27. K. I. Willig, J. Keller, M. Bossi, and S. W. Hell, “STED Microscopy Resolves Nanoparticle Assemblies,” *New Journal of Physics* 8, no. 6 (2006): 106, https://doi.org/10.1088/1367-2630/8/6/106.

28. M. C. Jenkins and S. U. Egelhaaf, “Confocal Microscopy of Colloidal Particles: towards Reliable, Optimum Coordinates,” *Advances in colloid*

and interface science 136, no. 1-2 (2008): 65–92, https://doi.org/10.1016/j.cis.2007.07.006.

29. V. Prasad, D. Semwogerere, and E. R. Weeks, "Confocal Microscopy of Colloids," *Journal of Physics: Condensed Matter* 19, no. 11 (2007): 113102, https://doi.org/10.1088/0953-8984/19/11/113102.

30. A. V. Blaaderen and A. Vrij, "Synthesis and Characterization of Colloidal Dispersions of Fluorescent, Monodisperse Silica Spheres," *Langmuir* 8, no. 12 (1992): 2921–2931, https://doi.org/10.1021/la00048a013.

31. N. A. M. Verhaegh and A. V. Blaaderen, "Dispersions of Rhodamine-Labeled Silica Spheres: Synthesis, Characterization, and Fluorescence Confocal Scanning Laser Microscopy," *Langmuir* 10, no. 5 (1994): 1427–1438, https://doi.org/10.1021/la00017a019.

32. A. van Blaaderen and P. Wiltzius, "Real-Space Structure of Colloidal Hard-Sphere Glasses," *Science* 270, no. 5239 (1995): 1177–1179, https://doi.org/10.1126/science.270.5239.1177.

33. A. Van Blaaderen, A. Imhof, W. Hage, and A. Vrij, "Three-Dimensional Imaging of Submicrometer Colloidal Particles in Concentrated Suspensions Using Confocal Scanning Laser Microscopy," *Langmuir* 8, no. 6 (1992): 1514–1517, https://doi.org/10.1021/la00042a005.

34. W. Man, M. Megens, P. J. Steinhardt, and P. M. Chaikin, "Experimental Measurement of the Photonic Properties of Icosahedral Quasicrystals," *Nature* 436, no. 7053 (2005): 993–996, https://doi.org/10.1038/nature03977.

35. S. Shahabi, L. Treccani, and K. Rezwan, "Amino Acid-Catalyzed Seed Regrowth Synthesis of Photostable High Fluorescent Silica Nanoparticles with Tunable Sizes for Intracellular Studies," *Journal of Nanoparticle Research* 17 (2015): 1–15, https://doi.org/10.1007/s11051-015-3072-8.

36. G. H. Bogush and C. F. Z. Iv, "Uniform Silica Particle Precipitation: an Aggregative Growth Model," *Journal of Colloid and Interface Science* 142, no. 1 (1991): 19–34, https://doi.org/10.1016/0021-9797(91)90030-C.

37. A. van Blaaderen, J. van Geest, and A. Vrij, "Monodisperse Colloidal Silica Spheres from Tetraalkoxysilanes: Particle Formation and Growth Mechanism," *Journal of colloid and interface science* 154, no. 2 (1992): 481–501, https://doi.org/10.1016/0021-9797(92)90163-G.

38. Q. Fan, Z. Li, Y. Li, et al., "Unveiling Enhanced Electrostatic Repulsion in Silica Nanosphere Assembly: Formation Dynamics of Body-Centered-Cubic Colloidal Crystals," *Journal of the American Chemical Society* 145, no. 51 (2023): 28191–28203, https://doi.org/10.1021/jacs.3c10817.

39. J. Wang, S. Hahn, E. Amstad, and N. Vogel, "Tailored Double Emulsions Made Simple," *Advanced Materials* 34, no. 5 (2022): 2107338, https://doi.org/10.1002/adma.202107338.

40. E. B. V. D. Wee, J. Fokkema, C. L. Kennedy, et al., "3D Test Sample for the Calibration and Quality Control of Stimulated Emission Depletion (STED) and Confocal Microscopes," *Communications Biology* 4, no. 1 (2021): 909, https://doi.org/10.1038/s42003-021-02432–3.

41. N. T. Urban, K. I. Willig, S. W. Hell, and U. V. Nägerl, "STED Nanoscopy of Actin Dynamics in Synapses Deep inside Living Brain Slices," *Biophysical Journal* 101, no. 5 (2011): 1277–1284, https://doi.org/10.1016/j.bpj.2011.07.027.

42. D. B. Allan, C. N. C. Keim C. M. van der Wel, and R. W. Verweij, soft-matter/trackpy: v0.6.4, 2024, https://doi.org/10.5281/zenodo.1213240.

43. J. C. Crocker and D. G. Grier, "Methods of Digital Video Microscopy for Colloidal Studies," *Journal of Colloid and Interface Science* 179, no. 1 (1996): 298–310, https://doi.org/10.1006/jcis.1996.0217.

44. A. UlugöL, J. Bückmann, R. Yang, et al., "Comparing Unsupervised Learning Methods for Local Structural Identification in Colloidal Systems," preprint arXiv (2025): arXiv:250907186, 10.48550/arXiv.2509.07186.

45. J. A. van Meel, L. Filion, C. Valeriani, and D. Frenkel, "A Parameter-Free, Solid-Angle Based, Nearest-Neighbor Algorithm," *The Journal of Chemical Physics* 136, no. 23 (2012): 234107.

46. P. J. Steinhardt, D. R. Nelson, and M. Ronchetti, "Bond-Orientational Order in Liquids and Glasses," *Physical Review B* 28, no. 2 (1983): 784.

47. W. Lechner and C. Dellago, "Accurate Determination of Crystal Structures Based on Averaged Local Bond Order Parameters," *The Journal of Chemical Physics* 129, no. 11 (2008): 114707.

48. J.-P. Baudry, A. E. Raftery, G. Celeux, K. Lo, and R. Gottardo, "Combining Mixture Components for Clustering," *Journal of Computational and Graphical Statistics* 19, no. 2 (2010): 332–353.

49. K. Shirk, C. Steiner, J. W. Kim, M. Marquez, and C. J. Martinez, "Assembly of Colloidal Silica Crystals inside Double Emulsion Drops," *Langmuir* 29, no. 38 (2013): 11849–11857, https://doi.org/10.1021/la4019986.

50. P. M. Naveenkumar, L. J. Roemling, U. Sultan, and N. Vogel, "Fabrication of Spherical Colloidal Supraparticles via Membrane Emulsification," *Langmuir* 40, no. 42 (2024): 22245–22255, https://doi.org/10.1021/acs.langmuir.4c02803.

51. R. Ohnuki, N. Kunimoto, Y. Takeoka, and S. Yoshioka, "Optical Characterization of Large Icosahedral Colloidal Clusters," *Particle & Particle Systems Characterization* 39 (2022): 2100257, https://doi.org/10.1002/ppsc.202100257.

52. P. K. Bommineni, J. Wang, N. Vogel, and M. Engel, "Entropic Trapping of Hard Spheres in Spherical Confinement," *Physical Review Letters* 134, no. 19 (2025): 198201, https://doi.org/10.1103/PhysRevLett.134.198201.

53. J. Lacava, P. Born, and T. Kraus, "Nanoparticle Clusters with Lennard-Jones Geometries," *Nano Letters* 12, no. 6 (2012): 3279–3282, https://doi.org/10.1021/nl3013659.

Supporting Information

Additional supporting information can be found online in the Supporting Information section.

Supporting File 1: adma72611-sup-0001-SuppMat.docx.
Supporting File 2: adma72611-sup-0002-HTML5genfile.txt.
Supporting File 3: adma72611-sup-0003-HTML5genfile2.txt.